Applied Catalysis B: Environmental 188 (2016) 87–97

Contents lists available at ScienceDirect

Applied Catalysis B: Environmental

journal homepage: www.elsevier.com/locate/apcatb

# Controlled synthesis of $BiVO_4$ photocatalysts: Evidence of the role of heterojunctions in their catalytic performance driven by visible-light

Osmando F. Lopes[a,b], Kele T.G. Carvalho[b], André E. Nogueira[b], Waldir Avansi Jr.[c], Caue Ribeiro[b,*]

[a] Departamento de Química, Universidade Federal de São Carlos—UFSCar, Rod. Washington Luiz, km 235, CEP 13565-905 São Carlos, SP, Brazil
[b] Laboratório Nacional de Nanotecnologia para o Agronegócio (LNNA)—Embrapa Instrumentação, Rua XV de Novembro, 1452, CEP 13560-970 São Carlos, SP, Brazil
[c] Departamento de Física, Universidade Federal de São Carlos, Rod. Washington Luiz, km 235, CEP 13565-905 São Carlos, SP, Brazil

ARTICLE INFO

*Article history:*
Received 7 December 2015
Received in revised form 20 January 2016
Accepted 26 January 2016
Available online 1 February 2016

*Keywords:*
$m$-$BiVO_4$/$t$-$BiVO_4$ heterostructure
Nanoparticles
Water decontamination
Visible-light
Photodegradation mechanism

ABSTRACT

Despite heterostructured semiconductors gaining attention as photocatalysts due to their improved activity compared to that of the isolated materials, the role of these heterojunctions in charge separation (electron/hole) remains unclear. Therefore, we studied these aspects in monoclinic/tetragonal $BiVO_4$ ($m$-$BiVO_4$/$t$-$BiVO_4$) heterostructures, which was chosen as an active material model under visible irradiation. The synthetic route was based on vanadium peroxo complex preparation as an intermediate step in structure formation using a hydrothermal process. When $V_2O_5$ was used at a molar ratio of 5:1 $H_2O_2$:(Bi + V) with 24 h of annealing, the $m$-$BiVO_4$/$t$-$BiVO_4$ heterostructure was obtained, and this material exhibited better photocatalytic performance in methylene blue degradation under visible irradiation than isolated phases. The HRTEM images revealed that heterostructured sample was composed of nanoparticles of $m$-$BiVO_4$ and $t$-$BiVO_4$ with size lower than 10 nm, the interface of $m$-$BiVO_4$/$t$-$BiVO_4$ was also evidenced. Surprisingly, despite the $t$-$BiVO_4$ structure being less active than $m$-$BiVO_4$, the heterostructures with a higher $t$-$BiVO_4$ content were more photoactive. The $m$-$BiVO_4$/$t$-$BiVO_4$ heterostructure showed no significant deactivation even after four successive re-uses for MB photodegradation. Oxidation mechanism of the MB dye was elucidated by mass spectroscopy. Indeed, the species scavenger trapping experimental results reveal the formation of a type-II heterostructure that led to an increase in the charge carrier lifetime, where the holes ($h^+$), superoxide anion radicals ($O_2^{-\bullet}$) and hydroxyl radicals ($^\bullet$OH) are the main active species.



## 1. Introduction

Semiconductors employed as photocatalysts that can be activated by visible radiation have attracted intense scientific interest due to their applications in heterogeneous photocatalysis, especially for the degradation of organic contaminants as well as for water splitting and artificial photosynthesis [1–8]. Among the various photocatalysts, bismuth vanadate ($BiVO_4$) is a promising $n$-type semiconductor candidate for these applications due to its narrow band gap of approximately 2.4–2.8 eV, nontoxicity, high chemical stability and photo stability, and its ability to absorb sunlight [1,9–12]. $BiVO_4$ exists in three different crystalline phases [13,14]. Among these phases, the monoclinic ($m$-$BiVO_4$) phase has been extensively studied due to its better photocatalytic performance under visible irradiation, which is primarily due to the lower and more suitable band gap (i.e., approximately 2.4 eV) [15,16].

Recently, our group demonstrated that the $m$-$BiVO_4$ photoactivity was limited by its inability to reduce $O_2$ to $O_2^{\bullet-}$ (superoxide radical) and trap the electron photogenerated on the conduction band (CB) [17]. Several strategies have been proposed to increase the performance of these photocatalysts [18–20] including doping [21–23], co-catalysts loading [24–26], and heterostructures formation [11,27–29]. The formation of heterojunctions between different phases of the same material is a promising approach for photocatalytic applications [30–33]. In addition, the formation of heterostructure between the monoclinic and tetragonal $BiVO_4$ phases is an interesting method for improving the photoactivity of these systems. In recent studies, different procedures for preparing $m$-$BiVO_4$/$t$-$BiVO_4$ heterostructure have been reported, and the

* Corresponding author.
*E-mail addresses:* caue.ribeiro@embrapa.com.br, caue1977@gmail.com (C. Ribeiro).

http://dx.doi.org/10.1016/j.apcatb.2016.01.065
0926-3373/

existence of a mixed phase resulted in a higher photocatalytic activity, which was due to the separation of photoinduced electron/hole pairs [30–34]. However, these mechanisms have not been identified, and a clear correlation between charge separation effects and the photodegradation paths has not been established.

Therefore, the aim of this study was to analyze the photodegradation mechanisms and the effects of charge transfer on enhancing the activity of $m$-$BiVO_4$/$t$-$BiVO_4$ heterostructures and correlate these factors to the structural features. A synthesis method based on the previous preparation of V peroxo complexes and crystallization using a hydrothermal process has been developed. The photocatalytic activity of the as-synthesized $BiVO_4$ pure and heterostructured samples were investigated for the photodegradation of MB dye in an aqueous solution, under visible irradiation.

## 2. Experimental

### 2.1. Synthesis of materials

The oxidant peroxide method (OPM) with crystallization under hydrothermal conditions is a good route for obtaining oxide semiconductors with desirable properties for photocatalytic applications because has several advantages for the synthesis of nanostructures [35–43]. This method was used to prepare $BiVO_4$ samples using different vanadium precursors (i.e., ammonium metavanadate ($NH_4VO_3$, ≥99.0%, Vetec—Sigma) or vanadium oxide ($V_2O_5$, ≥98.0%, Sigma)) with different hydrogen peroxide ($H_2O_2$, 30%, Synth) concentrations.

In a typical synthetic procedure [17], 0.69 $g$ of bismuth nitrate ($Bi(NO_3)_3{\cdot}5H_2O$, ≥99.0%, Aldrich) and 0.16 g of $NH_4VO_3$ or 0.13 g of $V_2O_5$ were dissolved in 40 mL of distilled water under vigorous stirring at room temperature. To study the effect of different hydrogen peroxide concentrations, $H_2O_2$ was added to the solution at a $H_2O_2$:M molar ratio equal to 5:1 or 10:1 (where M is the sum of the moles of Bi and V). The solution instantaneously exhibited a yellow color, which indicates the formation of the vanadium peroxo complex [44]. This complex was crystallized for 12 and 24 h at 120 °C under stirring using a homemade hydrothermal reactor. Then, the obtained material was cooled to room temperature, centrifuged, repeatedly washed to remove impurities and dried overnight at 50 °C.

The as-synthesized $BiVO_4$ samples are referred to as V$p$-C-$t$, where $p$ is the vanadium precursor ($p$ = 1 represents the $NH_4VO_3$ and $p$ = 2, the $V_2O_5$), C is the $H_2O_2$ concentration, and $t$ is the crystallization time.

### 2.2. Characterization of materials

The X-ray diffraction (XRD) patterns were recorded on a Shimadzu XRD 6000 diffractometer using Ni-filtered Cu kα (λ = 0.15406 nm) radiation operated at 30 kV and 30 mA in continuous scanning mode at a speed of 1° $min^{-1}$ and a step width of 0.02° from 10 to 70° 2θ. UV–vis diffuse reflectance spectra were recorded on a Varian model Cary 5G spectrometer from 200 to 800 nm to determine the band gap of the materials. The measurements were performed in total reflection mode with an integration cell containing MgO as a reference. To obtain the specific surface area (SSA) of the samples, $N_2$ adsorption analysis was performed at −196 °C using a Micrometrics ASAP 2000, and the respective SSA was obtained via BET modeling. Prior to the analyses, the samples were pre-treated (degasification) by heating at 80 °C under vacuum until reaching a degassing pressure lower than 10 μmHg. The zeta potential measurements were performed using Malvern—ZetaSizer model nano-ZS equipment with the catalyst in a water suspension (0.5 g $L^{-1}$).

The morphology and particles size of the samples were investigated using scanning electron microscopy (SEM) with a field emission gun (FEG) JEOL JSM 6701F. High resolution transmission electron microscopy (HRTEM FEI—TECNAI LaB6) operating at 200 kV was employed to verify the formation of heterostructures. TEM samples were prepared by wetting carbon-coated copper grids with a drop of colloidal alcoholic suspensions, followed by drying in air. Chemical surface analysis was performed on a K-Alpha XPS (Thermo Fisher 1 Scientific, UK) using Al Kα X-rays, vacuum >$10^{-8}$ mbar and charge compensation during measurements. The survey and high-resolution spectra were recorded using a pass energy of 1.0 and 0.1 eV at a resolution of 1 and 0.1 eV, respectively. The binding energy was referenced to the C 1s peak at 284.8 eV. The data analysis was performed using the CASA XPS software.

### 2.3. Photocatalytic performance

The photocatalytic activities of the as-prepared $BiVO_4$ samples were evaluated for the photodegradation of methylene blue (MB), which was used as a model organic dye pollutant. In a typical experiment, 10 mg of the as-prepared sample were added to 20 mL of a 10 mg $L^{-1}$ MB aqueous solution. These dispersions were stirred and exposed to visible radiation using six lamps (Osram, 15 W and maximum intensity at 440 nm) in a homemade photoreactor maintained at 18 °C. The details regarding the homemade photoreactor have already been published elsewhere [17]. The MB photodegradation was monitored based on its absorption maximum at 665 nm at regular time intervals using a UV–vis spectrophotometer (Shimadzu—1601PC) in absorbance mode. Prior to the experiment, the samples were maintained in contact with the MB dye solution for 12 h in the dark to achieve adsorption-desorption equilibrium. For comparative purposes, we performed photocatalytic experiments using the commercial $V_2O_5$ – the same reagent used as V source in the synthetic processes – and it had a negligible photocatalytic effect under visible irradiation, which is in agreement with observed results in our previous work [35].

To verify the MB dye photo-oxidation and the probable formation of byproducts during the catalytic process, a study using Mass Spectrometrer and Total Organic Carbon (TOC) analyses were performed. MB dye solution was monitored in a positive ion mode using an Electrospray Ionization Mass Spectrometrer (ESI–MS, Varian 310-MS). The formed byproducts were analyzed by introducing aliquots into the ESI source with a syringe pump at a flow rate of 20 mL $min^{-1}$. The spectra were obtained after 2 min of equipment stabilization. The mineralization degree of MB dye photocatalyzed by $m$-$BiVO_4$/$t$-$BiVO_4$ heterostructure (V2-5-24 sample) was evaluated by measuring the decay of dissolved organic carbon using a total organic carbon (TOC) analyzer (Sievers InnovOx, GE Analytical Instruments).

Additionally, two different methods were employed to investigate the MB photodegradation mechanism driven by the $BiVO_4$ photocatalysts. The first method consisted of adding reactive species scavengers directly to the $BiVO_4$-containing MB solutions. In this procedure, dimethyl sulfoxide (DMSO), silver nitrate ($AgNO_3$) or sodium oxalate (SO) was added as a scavenger for •OH radicals, conduction band (CB) electrons and valence band (VB) photogenerated-holes, respectively [45]. The second method consisted of indirectly detecting the amount of •OH radicals based on the technique described by Ishibashi and Fujishima [46,47], where an alkaline terephthalic acid (TA) solution instead of the MB solution was mixed with $BiVO_4$ in the photoreactor. TA readily reacts with •OH and forms a highly fluorescent product (i.e., 2-hydroxyterephthalic acid). This product has a fluorescence emission at approximately 425 nm, and its amount is proportional to the total amount of •OH radicals formed during the photocatalytic process [36]. The concentration of TA was set to $5 \times 10^{-4}$ mol $L^{-1}$

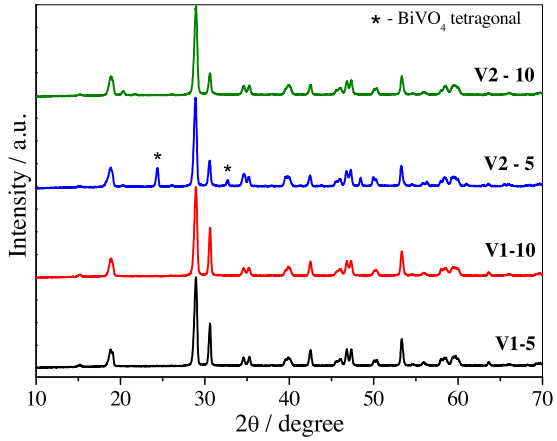


**Fig. 1.** XRD patterns of the as-synthesized $BiVO_4$ samples obtained using different precursors (V1 = $NH_4VO_3$ and V2 = $V_2O_5$) and $H_2O_2$ concentrations (5:1 and 10:1).

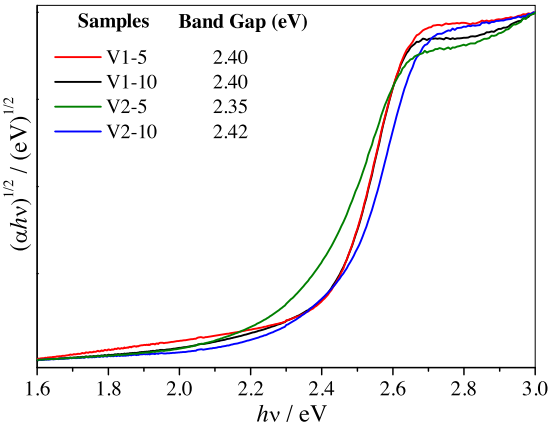


**Fig. 2.** Plot of $(\alpha h\nu)^{1/2}$ as a function of $h\nu$ from the UV–vis DRS curve of the as-prepared $BiVO_4$ using different precursors (V1 = $NH_4VO_3$ and V2 = $V_2O_5$) and $H_2O_2$ concentrations (5:1 and 10:1). The band gap values obtained from the Tauc equation[49] are shown in the inset.

in a dilute NaOH ($2 \times 10^{-3}$ mol $L^{-1}$) solution [36]. At regular time intervals, aliquots of the suspension were collected and analyzed in a LS 50B fluorescence spectrometer (Perkin Elmer). The fluorescence emission spectra were obtained at an excitation wavelength of 315 nm.

## 3. Results and discussion

### 3.1. Evaluation of vanadium precursor and $H_2O_2$ concentration in the $BiVO_4$ synthesis

Initially, the effects of the vanadium precursors and $H_2O_2$:M molar ratio (M is the sum moles of Bi and V) on the properties of the as-obtained materials were analyzed. The X-ray diffraction (XRD) patterns of the as-synthesized samples using different vanadium precursors and $H_2O_2$ concentrations are shown in Fig. 1. The results indicate that the pure *m*-$BiVO_4$ crystalline phase [JCPDS no. 014-0688] was formed in all of the samples obtained from the $NH_4VO_3$ precursor (V1) regardless of the $H_2O_2$ concentration. When the as-synthesized samples were obtained using the $V_2O_5$ precursor (V2), the main product was also the *m*-$BiVO_4$ phase. However, when the molar ratio of $H_2O_2$:M (M = Bi + V) decreased to 5, a small amount of the tetragonal $BiVO_4$ crystalline phase was identified by the appearance of diffraction peaks at $2\theta \approx 24.5^\circ$ and $32.7^\circ$ (marked with *), which correspond to the (200) and (112) planes [JCPDS no. 014-133], respectively. Based on the tetragonal $BiVO_4$ phase ($\% = I_{tetragonal(200)}/(I_{monoclinic(121)} + I_{tetragonal(200)} + I_{orthorhombic(001)})$ [34] from peaks intensities of XRD patterns, the V2-5 sample contains 75 and 19 wt.% of monoclinic and tetragonal $BiVO_4$, respectively. Additionally, the presence of a spurious orthorhombic $V_2O_5$ phase (~6 and 8 wt.%) was observed in the V2-5 and V2-10 samples, respectively, which was most likely due to some unreacted vanadium precursor that was identified based on the appearance of diffraction peaks at $2\theta \approx 20.3^\circ$ Corresponding to the (001) plane [JCPDS no. 01-076-1803].

These results reveal that the $H_2O_2$ concentration plays an important role in the synthesis of the tetragonal $BiVO_4$ phase, especially when $V_2O_5$ was used as the vanadium precursor. Nag et al. reported a similar effect, where the obtained $TiO_2$ crystalline phase depended on the $H_2O_2$:Ti ratio [48]. This result may be due to different solubilities of the precursors in water, where the solubility of the $V_2O_5$ precursor is almost negligible. In this case, the solubility is dependent on the vanadium peroxo complex formation due to the presence of $H_2O_2$.

The optical properties of the materials were studied using UV–vis diffuse reflectance spectroscopy (UV–vis DRS). The band gap energy ($E_g$) for a direct band gap semiconductor can be determined from the plots of $(\alpha h\nu)^{1/2}$ as a function of $h\nu$ (Fig. 2) originating from the Tauc equation [49]. The obtained band gap is very similar for all of the $BiVO_4$ samples and ranges from 2.35 to 2.42 eV. These results indicate that the different synthesis conditions did not lead to significant changes in the optical properties of these materials. As expected, these results also confirm that the photocatalysts can be activated by visible radiation [16,50].

The morphology and size of the $BiVO_4$ particles obtained using different synthesis conditions were examined by scanning electron microscopy (SEM). As shown in Fig. 3, all of the samples exhibited nanometer- and micrometer-sized particles in a range from 20 to 800 nm with sphere-like and worm-like shapes in large aggregates. However, the average particle size decreased, and the uniformity of size and shape increased (Fig. 3b and d) based on the $H_2O_2$ concentration for both cases (i.e., $NH_4VO_3$ and $V_2O_5$ precursors), which is most likely due to an increased vanadium peroxo complex formation that was induced by the increased $H_2O_2$ amount. This increased $H_2O_2$ amount controls the nucleation step and subsequent growth process. The role of the solubilization—reprecipitation processes during hydrothermal growth may be important. However, in this case, this aspect must be assumed to be an effect associated with the particle size after peroxo complex degradation because we can assume that it is the first step in annealing. It is important to note that despite the phase compositions among the samples being different (as shown in Fig. 1), no specific morphologies are associated with the tetragonal phase, indicating that both phases are formed together. All of the materials exhibited very low surface areas (below 1 $m^2$ $g^{-1}$), as expected [17,51].

The photocatalytic performance of the as-synthesized $BiVO_4$ using different precursors and $H_2O_2$ concentrations was investigated for the degradation of a MB dye solution under visible irradiation. Prior to the photocatalytic experiments, all of the materials were maintained in contact with the MB dye solution for 12 h in the absence of light to achieve adsorption-desorption equilibrium.

As shown in Fig. 4, the blank test in the absence of the photocatalysts indicates that the photolysis contribution can be ignored. Concerning the MB adsorption effect, the as-synthesized samples exhibited low adsorption capacities, ranging from 2 to 15%, as observed in Fig. S1. However, the V2-5 and V2-10 samples exhibited a higher MB adsorption capacity (ca. 10 and 15%, respectively) than the V1-5 and V1-10 samples (ca. 2 and 4%, respectively), indicating that the type of vanadium precursor ($V_2O_5$ or $NH_4VO_3$) can influence the physical and chemical properties that determine the adsorption potential. In fact, significant differences in one of the

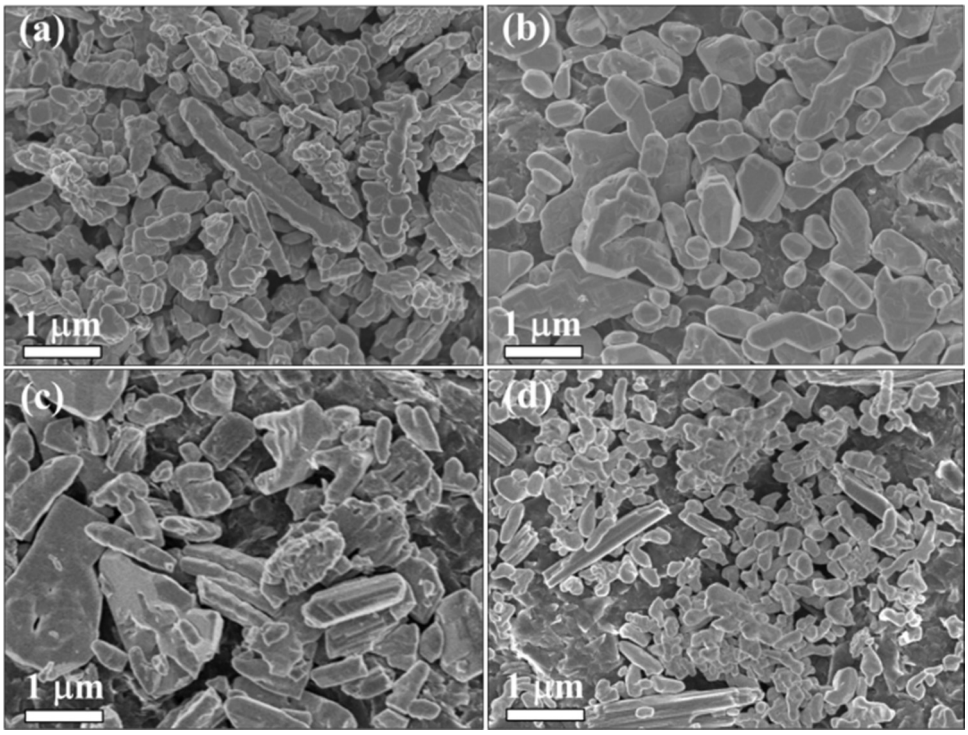


**Fig. 3.** Representative SEM images of the $BiVO_4$ samples obtained using different synthesis conditions: (a) V1-5, (b) V1-10, (c) V2-5, and (d) V2-10.

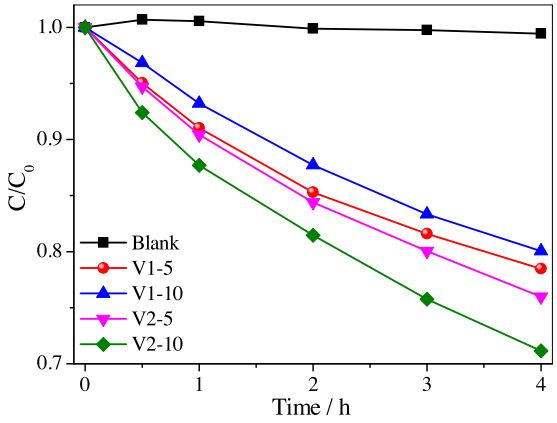


**Fig. 4.** Photodegradation of MB dye ($10\,mg\,L^{-1}$) catalyzed by the $BiVO_4$ samples under visible irradiation.

most important adsorption properties were observed, i.e., the surface charge of the particles measured by the zeta potential method at the natural pH of the MB solution (ca. 6.0) was highly positive (ca. + 33 mV) for V1-10 and negative (ca. −24 mV) for V2-10, which imposes an electrostatic repulsion and attraction to cationic MB dye, respectively [52]. The negative charge of the nanostructures, which was obtained by the OPM method, was also similar to the results observed in a previous study [35]. As shown in Table S1, the degradation rate constants ($k$) of the $BiVO_4$ photocatalysts followed the order V1-5 ≈ V1-10 < V2-5 < V2-10. The samples synthesized using $V_2O_5$ (as precursor) exhibited better photoactivity than the other materials, which is most likely due to better interaction with the MB dye.

It is well known that the tetragonal $BiVO_4$ crystalline phase is less active than the monoclinic one [1]. The V2-5 sample exhibited a high activity despite containing 19 wt.% of the tetragonal phase. Therefore, the relatively high activity of the V2-5 sample is most likely related to the formation of $m$-$BiVO_4$/$t$-$BiVO_4$ heterojunctions because a simple physical mixture of both phases could exhibit a lower activity than pure $m$-$BiVO_4$. The formation of heterostructures between different phases of the same semiconductor is possible because the phases possess valence and conduction bands with suitable positions [53–55]. Titanium oxide ($TiO_2$ P25—Degussa) is a classic example of a heterostructured photocatalyst (i.e., an ideal mixed formed consisting of anatase and rutile phases), which has greater photoactivity than its isolated constituent phases [55,56]. Similarly, Ding et al. demonstrated that the relative positions of the valence and conduction bands and the Fermi energy levels of the monoclinic and tetragonal $BiVO_4$ phases are appropriated for the formation of one type-II heterostructure that is capable of promoting an effective separation of the photogenerated charges [57]. However, the ratio between the different phases in a heterostructure is a fundamental parameter that can be tuned to optimize its photocatalytic performance.

### 3.2. Study of $BiVO_4$ heterostructured formation as a function of synthesis time

As discussed above, the $BiVO_4$ samples that were prepared using $V_2O_5$ as a precursor exhibited higher adsorption and photoactivity for MB dye removal than the $BiVO_4$ samples prepared using the $NH_4VO_3$ precursor. The V2-5 sample contained mixed phases (i.e., $m$-$BiVO_4$/$t$-$BiVO_4$), and its higher photoactivity can be directly related to the formation of a type-II heterostructure between the constituent phases. The photocatalytic performance of heterostructures has been previously studied, and an appropriate amount of the mixed phases appears to be a key factor in the development of a photocatalyst with a higher performance [33,41,58–60].

To optimize and evaluate the appropriate synthetic conditions for obtaining a heterostructure with better photocatalytic performance, the crystallization time was also evaluated. The time was increased from 12 to 24 h using both vanadium precursors (i.e., $NH_4VO_3$ and $V_2O_5$) with a fixed $H_2O_2$:M molar ratio equal to 5:1. For comparative purposes, the V2-10-24 sample was also synthe-

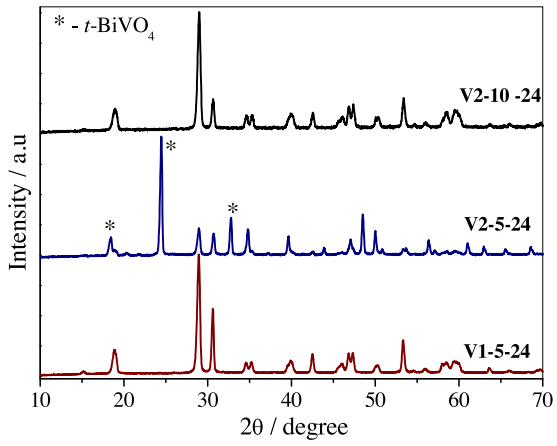


**Fig. 5.** Powder XRD patterns of the as-synthesized $BiVO_4$ samples.

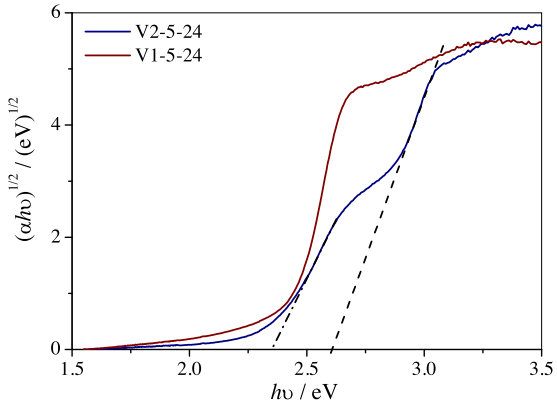


**Fig. 6.** Plots of $(\alpha h\upsilon)^{1/2}$ as a function of the photon energy ($h\upsilon$) obtained using the Tauc equation[49] from the DRS spectra for the V1-5-24 and V2-5-24 samples.

sized, since the V2-10 sample showed a good photoactivity (Fig. 4). The XRD patterns for these samples are shown in Fig. 5. When the $NH_4VO_3$ precursor was employed (i.e., V1-5-24 sample), pure *m*-$BiVO_4$ was obtained. Therefore, the increase in the synthesis time did not cause significant structural changes compared to the synthesis performed for 12 h under the same conditions (V1-5 sample). This result was also observed for the V2-10-24 sample, in which was obtained only $BiVO_4$ in monoclinic phase. However, when the $V_2O_5$ precursor was used with a fixed $H_2O_2$:M molar ratio equal to 5:1 (i.e., V2-5-24 sample), a DRX pattern corresponding to mixed phases consisting of monoclinic (~ 20 wt.%) and tetragonal (~75 wt.%) $BiVO_4$ crystalline phases were observed, and *t*-$BiVO_4$ appears to be the major crystalline phase.

For the V2-5-24 sample, the presence of a spurious $V_2O_5$ phase (~5 wt.%) was also observed. According to the XRD results shown in Figs. 1 and 5, the increase in the synthesis time led to a significant change in the ratio between the monoclinic and tetragonal phases (i.e., increase in the percentage of the *t*-$BiVO_4$ phase from 19 to 75%).

The optical properties of the materials were investigated using UV–vis DRS (Fig. 6). The V1-5-24 sample exhibited a band gap value of 2.42 eV, which is similar to that of the V1-5 sample (inset on Fig. 2). For the V2-5-24 sample, two band gaps were observed and are highlighted by dashed lines in Fig. 6. This result confirms the coexistence of two crystalline phases of $BiVO_4$. The band gap values were determined to be 2.35 and 2.61 eV, and these values are similar to those reported for the *m*- and *t*-$BiVO_4$ phases, respectively [1].

Based on the SEM images, the V1-5-24 and V2-5-24 samples (Fig. 7) exhibited morphologies that were similar to those of their corresponding samples treated for 12 h (i.e., the V1-5 and V2-5 samples, respectively). However, the increase in the hydrothermal treatment time led to a higher uniformity in the shape and size of the particles, and smaller particle sizes were obtained. The SSA data for both samples obtained using the BET model were 0.63 $m^2\ g^{-1}$ and 0.26 $m^2\ g^{-1}$ for the V1-5-24 and V2-5-24 samples, respectively. By considering the intrinsic error of the technique, these values can be assumed to be equal and not significant parameter for this material under these specific synthetic conditions.

TEM and HRTEM images of the V1-5-24 and V2-5-24 samples are shown in Fig. 8. The V1-5-24 sample (Fig. 8a and b) consists of agglomerates formed by a large number of well faceted $BiVO_4$ nanoparticles with size lower than 10 nm. This result is surprising because by SEM images analysis of the V1-5-24 sample (Fig. 7), it was observed only micrometric particles with smooth surface. Therefore, the SEM analysis for this kind of samples is not completely proper. HRTEM image of the V1-5-24 sample showed interlayer distance of 0.31 nm, which can be assigned to (121) plane of the monoclinic $BiVO_4$ phase. This result brings a new insight about the performance of the $BiVO_4$ photocatalysts, since the formation of heterostructures between the nanoparticles can be more effective than the formation with micrometric particles.

As shown in Fig. 8c, the V2-5-24 sample exhibited similar morphological characteristics to that of the V1-5-24 sample, i.e. the presence of well faceted nanoparticles with size lower than 10 nm. Nevertheless, HRTEM image of this sample (Fig. 8d) showed the coexistence of the nanoparticles of $BiVO_4$ in monoclinic and tetragonal phases in the same region, which were identified by their interlayer distances of 0.31 nm referent to (121) plane and 0.23 nm referent to (301) plane, respectively. This result is an indicative of the formation of heterojunctions between *m*-$BiVO_4$ and *t*-$BiVO_4$.

XPS analysis was performed to investigate the surface composition and chemical state of the elements of the V1-5-24 and V2-5-24 samples, and the results are shown in Fig. 9. From the survey spectra (Fig. 9a), the presence of Bi, V, O and C (this was used as an internal reference) were confirmed in both samples without any contamination. The XPS spectra contained the characteristic spin-orbit splitting of the Bi $4f_{5/2}$ and Bi $4f_{7/2}$ signals (Fig. 9b), V $2p_{1/2}$ and V $2p_{3/2}$ signals (Fig. 9c), and O 1s peak (Fig. 9d) [14,61,62]. The binding energies of Bi 4f and V 2p and the difference between the low and high spin states are provided in Table S2. Slight shifts in the binding energies were observed among the $BiVO_4$ samples (Fig. 9 and Table S2) because the V1-5-24 sample contains a pure *m*-$BiVO_4$ phase, whereas the V2-5-24 sample contains a mixture of *m*-$BiVO_4$ and *t*-$BiVO_4$ phases. As expected, the samples exhibit differences in their chemical environments due to the different crystal structures, which is in agreement with previous results [13,14]. It is important to note that the O 1s signal of the samples was a wide and slightly asymmetrical peak, indicating that other oxygen species are present in the surface region, and these oxygen species might be hydroxyl oxygen and adsorbed oxygen on the surface of $BiVO_4$ [13].

The photocatalytic performance of the V1-5-24, V2-5-24 and V2-10-24 samples was probed by MB dye photodegradation under visible irradiation, and these results were compared to the results obtained using the V1-5 and V2-5 samples (Figs. 10 and S2). For the samples obtained using the $NH_4VO_3$ precursor (V1-5 and V1-5-24), the synthesis time did not influence the adsorption or photocatalytic performance. Both samples exhibited an approximately 5 and 20% MB removal for adsorption and photodegradation, respectively. It was also observed that the increase in hydrothermal treatment time to obtain the V2-10-24 sample did not cause any difference in its photoactivity when compared to V2-10 sample. However, for the samples V2-5 and V2-5-24, the synthesis time

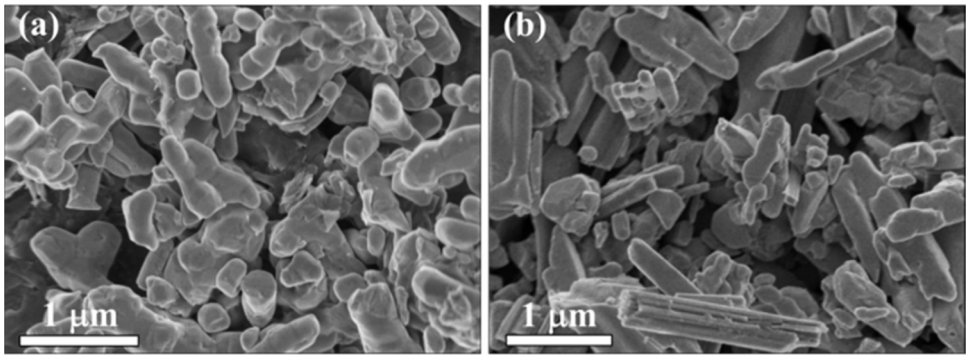


**Fig. 7.** Representative SEM images of the (a) V1-5-24 and (b) V2-5-24 samples.

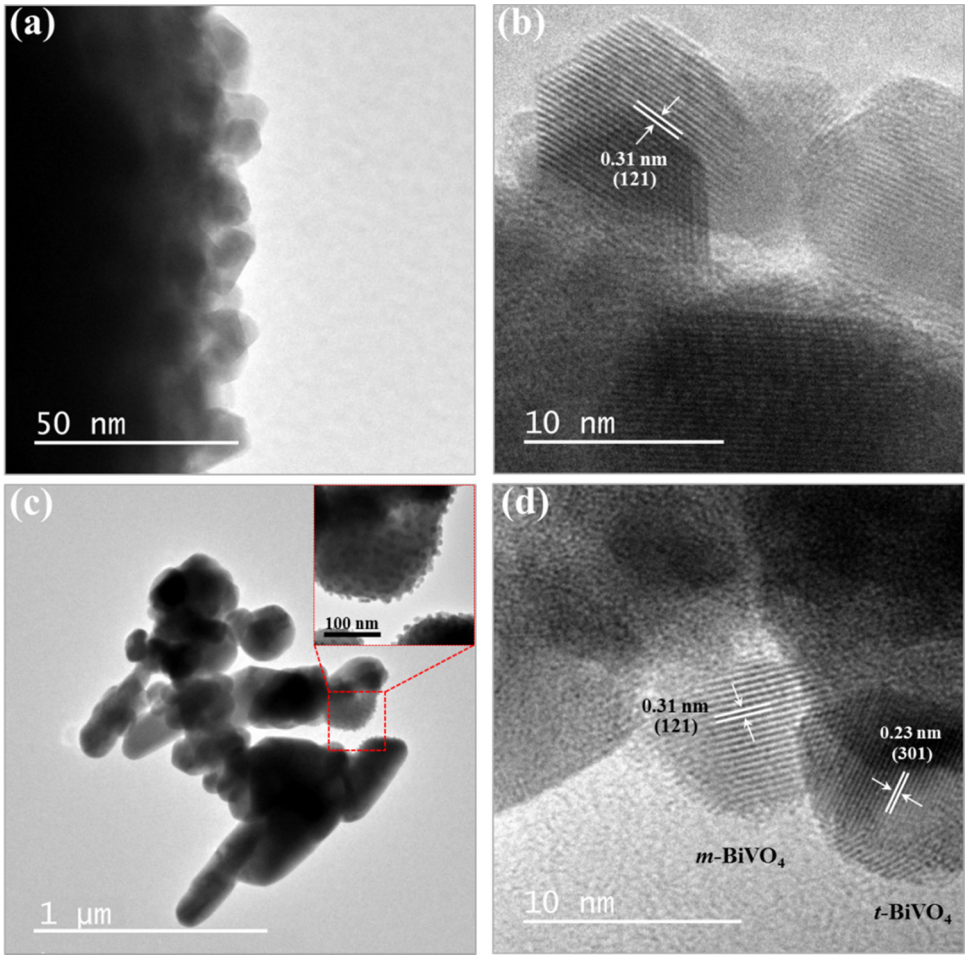


**Fig. 8.** TEM and HRTEM images of the (a-b) V1-5-24 and (c-d) V2-5-24 samples.

played a fundamental role in the preparation of photocatalysts with different phases compositions and different photocatalytic performances. The V2-5-24 sample exhibited a higher MB adsorption (approximately 45%) and a higher catalytic activity (approximately 60%) for MB photodegradation than the V2-5 sample, which exhibited an adsorption and photodegradation efficiency of 15 and 20%, respectively. This trend was consistent with the results for the rate constant ($k$) analysis, where the V2-5-24 sample exhibited a rate constant for MB photodegradation 3.6 times higher than that observed for V2-5 (Table S3). The higher photoactivity of the V2-5-24 sample was unexpected because in this sample, tetragonal $BiVO_4$ is the major crystalline phase, which is less active than the $m$-$BiVO_4$ phase. The $m$-$BiVO_4$/$t$-$BiVO_4$ heterojunctions lead to the efficient separation of the electron/hole pair (i.e., an increase in lifetime of charge carriers). Therefore, this result is surprising because it is expected that an efficient heterojunction formed by this system was composed of $m$-$BiVO_4$ as the major crystalline phase [63]. This result indicates that the $t$-$BiVO_4$ crystalline phase in the V2-5-24 sample was more photoactive. The origin of great increase in the adsorption capacity of the V2-5-24 sample (Fig. S2) can be related to its higher content of tetragonal phase, since Zhang et al. have been stablished that $BiVO_4$ in tetragonal phase shows a higher affinity to MB dye than the monoclinic one [64].

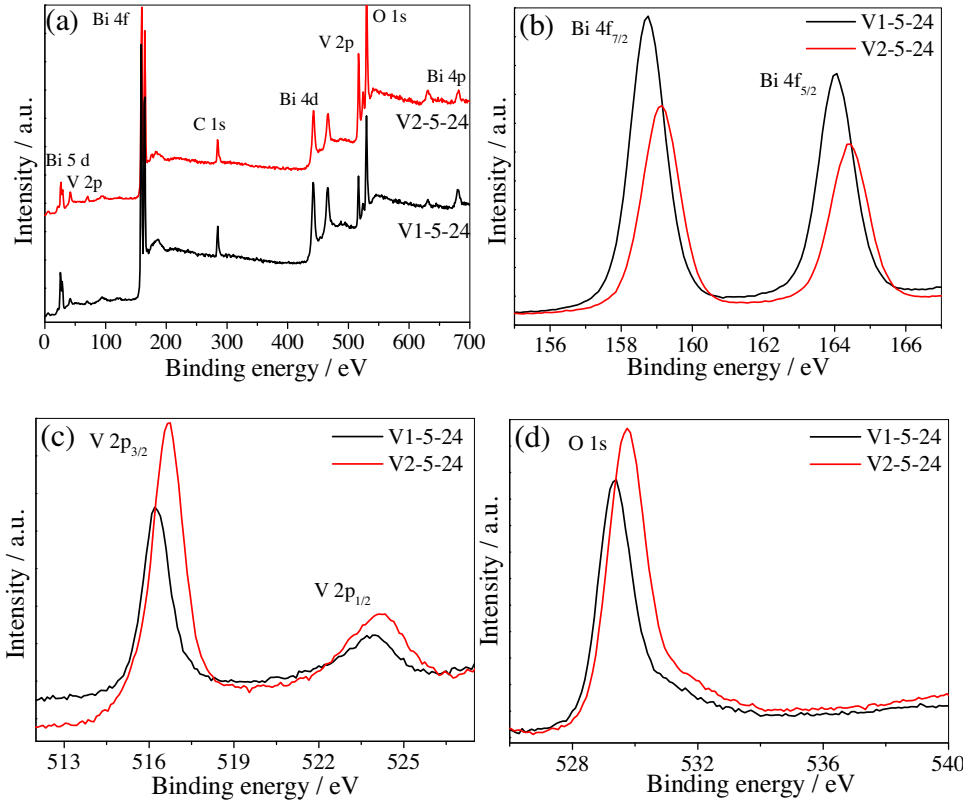


**Fig. 9.** X-ray photoelectron spectra of the V1-5-24 and V2-5-24 samples. (a) Survey spectra, (b) high-resolution spectra of Bi 4f, (c) high-resolution spectra of V 2p, and (d) high-resolution spectra of O 1s.

**Table 1**
First-order rate constants for the MB photodegradation tests performed under visible irradiation in the presence and absence of a sacrificial reagent ($Ag^+$).

| Sample | $k \times 100$ ($h^{-1}$) | $k_{Ag} \times 100$ ($h^{-1}$)[a] |
|---|---|---|
| V1-5-24 | 9.8 | 17.0 |
| V2-5-24 | 23.9 | 18.7 |

[a] $k_{Ag}$ is the rate constants for reaction in the presence of $Ag^+$.

Despite the fact that our results indicate that the *m*-$BiVO_4$/*t*-$BiVO_4$ heterojunctions are the main reason for the higher photoactivity of the V2-5 and V2-5-24 samples, an investigation of the influence of the heterojunctions on the photocatalytic performance was performed because the formation of a heterojunction can reduce the recombination rate of electron/hole pairs, which can increase the photocatalytic activity [65,66]. An analysis of the increase in the photoactivity associated with electron acceptors indirectly indicates the recombination rate of the structure. A good sacrificial reagent to use as an electron acceptor is $Ag^+$ ($Ag^+$/Ag 0.799 V vs NHE) because this ion can be spontaneously reduced at a high reduction potential [67,68]. Therefore, MB dye photodegradation tests in the presence or absence of $Ag^+$ ions were carried out (Fig. 10b). To quantitatively evaluate the influence of photogenerated electrons, a first-order kinetic model of the photodegradation data was applied (Fig. S3), and the kinetic constants ($k$) for the reaction are shown in Table 1. For the V1-5-24 sample, the addition of $Ag^+$ in the photocatalytic tests increased the MB degradation efficiency. The degradation percentage increased from 29 to 46% with the addition of $Ag^+$, and the $k$ value for the process containing $Ag^+$ was 1.7 times higher than that of the process performed in the absence of $Ag^+$. Therefore, the effect of the electron acceptor ($Ag^+$) increased the electron/hole pair lifetime, which significantly increased the efficiency of the photocatalytic process for the samples containing the *m*-$BiVO_4$ pure phase, as observed in our previous study [17].

A different effect was observed for the V2-5-24 sample compared to the V1-5-24 sample, where the addition of $Ag^+$ in the photocatalytic tests decreased the photoactivity of the sample. The rate constant of MB photodegradation for the V2-5-24 sample with $Ag^+$ was approximately 1.3 times lower than that in the absence of $Ag^+$. This result indirectly indicates that an efficient heterojunction was formed between the monoclinic and tetragonal $BiVO_4$ phases because $Ag^+$ did not increase the efficiency of the photodegradation process. However, the decrease in the photoactivity of the V2-5-24 sample in the presence of $Ag^+$ is related to the adsorption of Ag metal in actives sites liable for the adsorption of MB dye, which were created during visible irradiation leading to $Ag^+$ reduction [69].

Additionally, the formation and effect of the *m*-$BiVO_4$/*t*-$BiVO_4$ heterojunctions in the V2-5-24 sample were studied by analyzing the photocatalytic performance of a physical mixture (PM) prepared by mixing 75 wt.% of *t*-$BiVO_4$, 20 wt.% of *m*-$BiVO_4$ and 5 wt.% of $V_2O_5$ (Fig. S4). The *t*-$BiVO_4$ samples, which were employed as reference compounds, were prepared using the hydrothermal method reported by Guo et al. [14]. In summary, the photocatalytic performances of the as-prepared samples were in the following order: V2-5-24 (*m*-$BiVO_4$/*t*-$BiVO_4$) > *m*-$BiVO_4$ > PM > *t*-$BiVO_4$ (Fig. S4). Interestingly, the PM sample exhibited a lower photoactivity than the V2-5-24 sample. Therefore, these results confirm that V2-5-24 is not a physical mixture, rather than contains junctions between the constituent phases that result in a higher photoactivity due to the increased in the lifetime of electron/hole pairs. In addition, the PM sample exhibited an intermediate photoactivity that was between *m*-$BiVO_4$ and *t*-$BiVO_4$, indicating that its photoactivity is only a linear combination the photoactivity of the isolated phases.

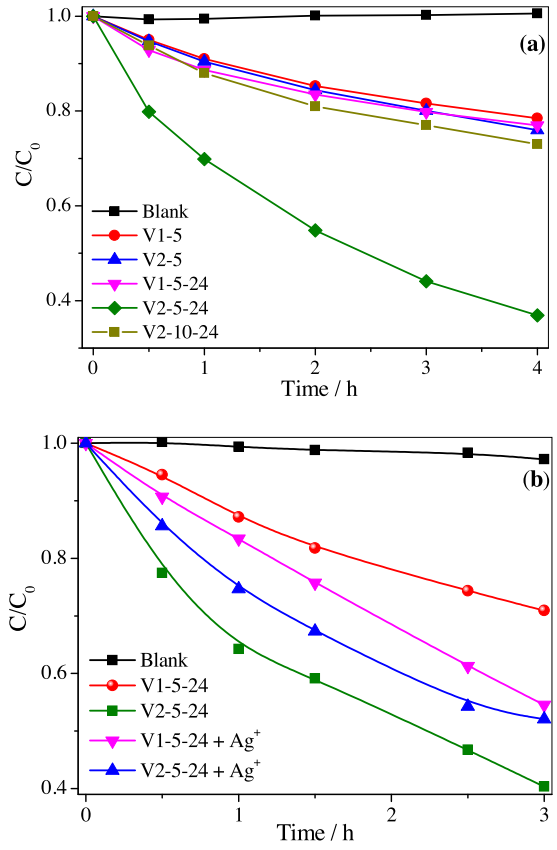


**Fig. 10.** (a) MB dye photodegradation catalyzed by the as-synthesized samples as a function of time under visible irradiation. (b) Photodegradation kinetics of MB catalyzed by the V1-5-24 and V2-5-24 samples with and without $Ag^+$ ($AgNO_3$, 20 mmol $L^{-1}$).

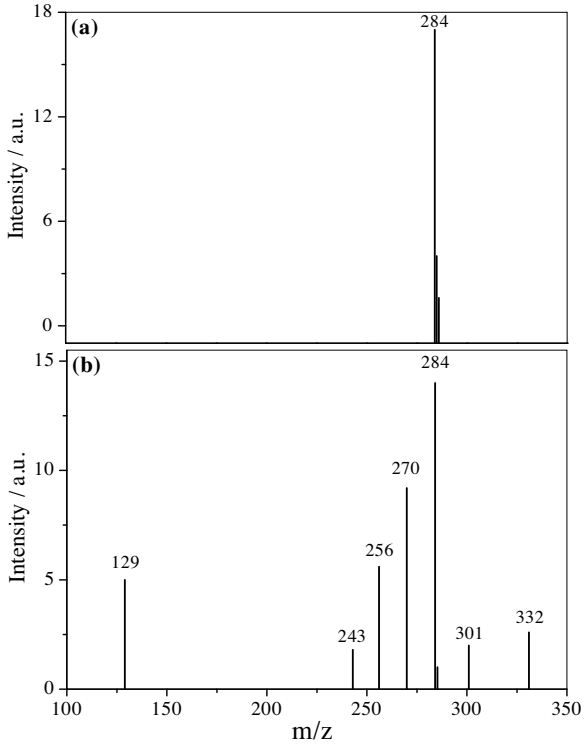


**Fig. 11.** ESI mass spectra of (a) MB dye pure and (b) catalyzed by the V2-5-24 sample for 3 h under visible irradiation.

**Table 2**
Rate constant of •OH radical formation by the as-synthesized $BiVO_4$ samples. The *k* values from Tables S1 and S3 are reproduced to facilitate comparison.

| Sample | *k* | $k_{OH}$ |
|---|---|---|
| V1-5 | 5.9 | 19.6 |
| V1-10 | 5.6 | 20.5 |
| V2-5 | 6.6 | 44.7 |
| V2-10 | 7.4 | 97.4 |
| V1-5-24 | 6.1 | 32.3 |
| V2-5-24 | 24.2 | 55.6 |

To elucidate the photo-oxidation of MB dye, it was performed the analysis of the MB solution before and after the photocatalytic experiments catalyzed by *m*-$BiVO_4$/*t*-$BiVO_4$ heterostructure using mass spectrometry (ESI–MS), depicted in Fig. 11. The ESI–MS spectrum obtained from the standard MB solution exhibited only a strong signal of mass/charge (*m*/*z*) ratio at 284, which is assigned to MB structure without any oxidation. After irradiation of the MB solution (catalyzed by *m*-$BiVO_4$/*t*-$BiVO_4$ heterostructure), mass spectrum revealed several peaks with *m*/*z* equal to 332, 301, 284, 270, 256, 243 and 129. The signals at *m*/*z* = 301 and 332 regard to one and three hydroxylation in the aromatic ring of MB, respectively [70–73]. The process of MB hydroxylation confirms that •OH radical played an important role for MB photodegradation. The signals of *m*/*z* = 270, 256 and 243 are referent to cleavage of one or more methyl groups substituent on the amine groups of MB and these species are azure B, azure A and azure C, respectively [74]. The signal of *m*/*z* = 129 is referent to cleavage of ring aromatic due to attack of species actives photogenerated in the presence of *m*-$BiVO_4$/*t*-$BiVO_4$ heterostructure [70–73].

Further, to confirm the efficiency of V2-5-24 sample to reduce the dissolved organic carbon in MB dye solution, its content was measured by TOC analyzer after 3 h under visible irradiation. It was observed that MB dye was 65% mineralized to $CO_2$ and $H_2O$ by V2-5-24 sample. This result evidences that the photocatalytic process proposed in this study was effective not only for the color removal, but also to reduce the organic content of the MB dye solution.

The stability of the catalyst is a fundamental property for its practical application for several catalytic cycles without loss in its efficiency. Therefore, the photostability of the *m*-$BiVO_4$/*t*-$BiVO_4$ heterostructure was evaluated by performing recycling experiments for five times under the same conditions used in the MB dye photodegradation tests. After each reaction cycle, the sample was separated from the MB solution by centrifugation, and placed immediately in contact with a freshly prepared MB solution. As shown in Fig. S5, the photocatalytic performance of *m*-$BiVO_4$/*t*-$BiVO_4$ heterostructure was kept even after four cycles, exhibiting only a slight decrease after fourth cycle.

### 3.3. Investigation of photodegradation mechanism and charge transfer

Despite the interesting and promising photocatalytic performance of the studied materials, a deeper analysis is required to elucidate the mechanism involved in the photocatalytic process. To evaluate the mechanism of MB photodegradation driven by the as-synthesized photocatalysts and the importance of pollutant degradation due to the formation of active radical species, such as •OH and $O_2^{\bullet -}$, the •OH radicals was detected using a method proposed by Ishibashi et al. [46,47] and discussed in detail by our group [36,58].

The rate constant formation of the •OH radicals is shown in Table 2 and Fig. S6. The efficiency of •OH radical formation can be represented by the $k_{OH}$ values listed in Table 2. The observed trend in the photoactivity of the samples obtained using the $NH_4VO_3$ precursor (V1-5, V1-10 and V1-5-24) for MB dye degradation was the

same as that observed for •OH radical formation (i.e., V1-5 ≈ V1-10 < V1-5-24), which indicates that an indirect mechanism plays a key role in the photoactivity. The trend of $k$ and $k_{OH}$ observed to reaction catalyzed by the V1 samples can be better analyzed in Fig. S7a. In fact, the pollutant photodegradation via an indirect mechanism (i.e., attack by •OH radical) catalyzed by the $m$-$BiVO_4$ phase has been previously observed by our group [17]. However, the observed trend for the efficiency of •OH radical formation over the samples obtained using the $V_2O_5$ precursor (V2-5, V2-10, V2-5-24) was different when compared to their photoactivity for MB dye photodegradation. The order observed in the photoactivity was as follows: V2-5 ≤ V2-10 < V2-5-24. However, the efficiency of •OH radical formation was as follows: V2-5 ≤ V2-5-24 < V2-10. The relationship between $k$ and $k_{OH}$ to reaction catalyzed by the V2 samples can be better analyzed in Fig. S7b. These results indicate that the V2-10 sample led the MB dye photodegradation primarily via an indirect mechanism (i.e., the •OH radical was the major active species in the process catalyzed by V2-10). The V2-10 sample exhibited a $k_{OH}$ value that was 1.8 times higher than that of the V2-5-24 sample, and for the rate constant of MB photodegradation, the V2-5-24 sample exhibited a $k$ value that was 3.3 times higher than that of V2-10. Therefore, despite the V2-5 and V2-5-24 samples (heterojunctions) producing •OH radicals, the indirect mechanism was not the main mechanism in MB dye degradation for these samples.

Additionally, to understand the photocatalytic mechanism of the reaction catalyzed by $m$-$BiVO_4$/$t$-$BiVO_4$ (V2-5-24), we evaluated the effects of the addition of three different reactive scavenger species (i.e., $Ag^+$ (strong oxidant, CB electrons acceptor), DMSO (a •OH scavenger) and sodium oxalate (SO, a VB holes photogenerated scavenger)) to the MB solution during the photocatalysis experiments [45,75,76]. Dissolved oxygen is considered to be a photogenerated electron scavenger that inhibits fast charge carrier recombination, resulting in the formation of a superoxide radical ($O_2^{-\bullet}$), which is important for some photodegradation processes [77]. Therefore, a rational approach for evaluating the importance of $O_2^{-\bullet}$ is to scavenge it with $Ag^+$ (previously shown in Fig. 10b) [45,76]. Therefore, if the photodegradation process is driven by $O_2^{-\bullet}$ radicals, the reaction rate should be substantially less with the addition of $Ag^+$. However, if the •OH radical or a direct degradation mechanism (i.e., pollutants are directly attack by VB holes) plays a major role in the photodegradation process, the reaction rate should decrease in the presence of excess DMSO and/or SO, respectively [45,76,78].

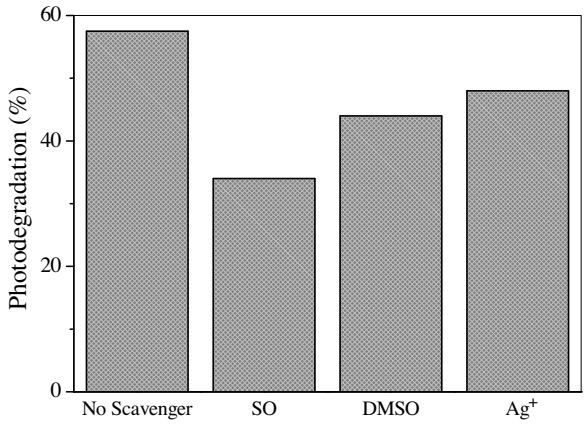


**Fig. 12.** MB dye photodegradation percentage catalyzed by the V2-5-24 sample with different scavengers during 2.5 h of visible irradiation.

As shown in Figs. 12 and S8, the addition of excess SO (10 mol $L^{-1}$) significantly inhibited the photodegradation percentage of MB dye compared to that with no scavenger under the same conditions from 59 to 34%. The rate constant decreased by approximately 50% (Fig. S7), indicating that the VB photogenerated holes and/or •OH active species play a crucial role in the MB photooxidation process. To separate the effects of •OH and the VB photogenerated holes, DMSO was employed as a selective scavenger for •OH. Excess DMSO in the MB solution capture all of the •OH radicals produced during the photocatalytic process [78]. As shown in Fig. 12, the use of excess DMSO resulted in slight decrease in the photodegradation percentage from 54 to 45% after 2.5 h of exposure to visible irradiation (the rate constant decreased by 25%, Fig. S8). Therefore, the direct mechanism plays a more important role than the indirect mechanism in the MB dye photodegradation process catalyzed by the V2-5-24 sample even though both mechanisms have a significant role. This result is in agreement with the result obtained for •OH radical formation via the terephthalic acid method.

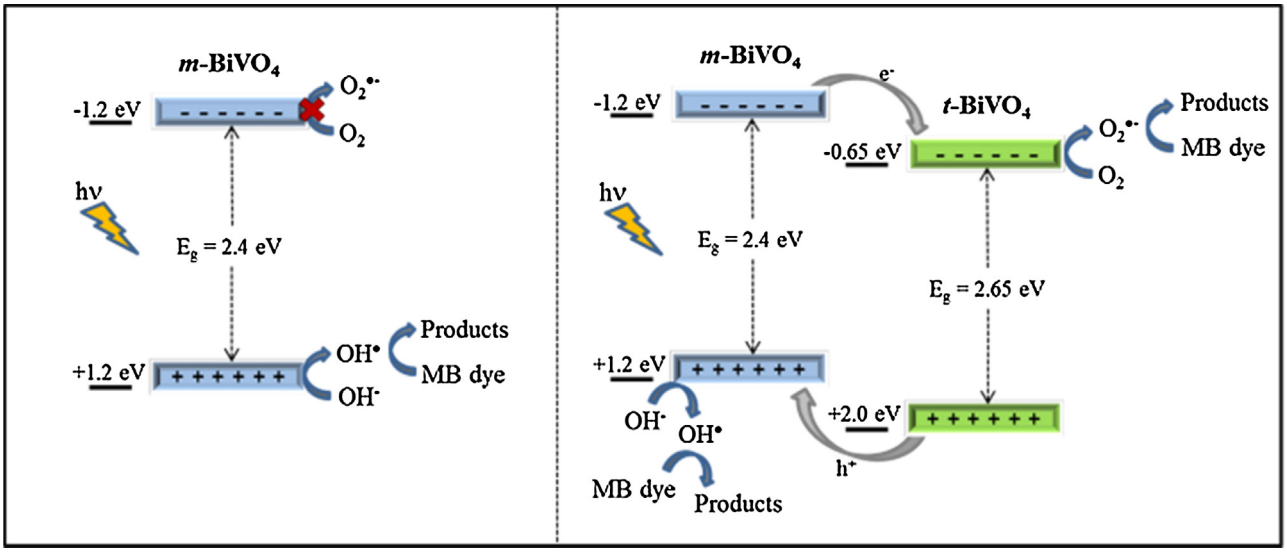


**Fig. 13.** Charge transfer between the monoclinic and tetragonal $BiVO_4$ phases in the heterostructure, and the VB and CB values were obtained by VB-XPS in the solid state under vacuum.

As previously shown in Figs. 10 b and 12, excess of $Ag^+$ in the MB solution resulted in a decrease in the photodegradation percentage from approximately 60–48% after 3 h of exposure to visible radiation (the rate constant decreased by 22%). Therefore, in contrast to pure *m*-$BiVO_4$, the *m*-$BiVO_4$/*t*-$BiVO_4$ heterostructured sample has a conduction band edge with a sufficiently high potential or lifetime of photogenerated electron to reduce the dissolved oxygen. Therefore, the superoxide radical ($O_2^{-\bullet}$) plays also an important role in the MB photodegradation mechanism catalyzed by the *m*-$BiVO_4$/*t*-$BiVO_4$ heterostructure sample.

To understand the photodegradation mechanism and charge transfer between the phases contained in the V2-5-24 heterostructure sample, the valence band (VB) was determined using XPS and compared to that of V1-5-24 (Fig. S9). The spectrum thresholds of the V1-5-24 and V2-5-24 samples are 1.2 and 2.0 eV, respectively. The value of VB top in V1-5-24 was consistent with that of the *m*-$BiVO_4$ phase, as previously reported [13]. The *t*-$BiVO_4$ phase has a less positive VB top (0.9 eV) than the *m*-$BiVO_4$ phase (1.1 eV), as reported by Li et al. [13]. Therefore, the V2-5-24 sample exhibited a VB top value that was much higher than expected compared to those of the *m*- and/or *t*-$BiVO_4$ phases, indicating that a heterojunction forms between the phases resulting in a shift in the VB top of both phases.

In summary, according to our results, the mechanism for the photodegradation of organic pollutants on the surface of the pure *m*-$BiVO_4$ photocatalyst occurs primarily via an indirect mechanism (i.e., $^\bullet$OH radical generation and attack). However, the *m*-$BiVO_4$/*t*-$BiVO_4$ heterostructure led the photodegradation of pollutants via direct and indirect mechanisms (i.e., by the formation and attack of $^\bullet$OH and $O_2^{-\bullet}$ radicals and direct VB hole oxidation). Therefore, the great increase in *m*-$BiVO_4$/*t*-$BiVO_4$ heterostructure photoactivity can be related to its ability to activate three different photodegradation paths. The main photodegradation mechanism of *m*-$BiVO_4$ is compared to the mechanism and charge transfer of the enhanced photocatalytic performance of the *m*-$BiVO_4$/*t*-$BiVO_4$ heterostructure in Fig. 13.

## 4. Conclusions

In summary, the formation of heterostructures between different phases of the same semiconductor provides a viable alternative for improving the photocatalytic performance. Using the proposed synthesis method, a pure *m*-$BiVO_4$ phase as well as *m*-$BiVO_4$/*t*-$BiVO_4$ heterostructures were prepared by controlling the synthesis parameters. The heterostructured samples are composed of nanoparticles of *m*-$BiVO_4$ and *t*-$BiVO_4$ with size lower than 10 nm, and the probable interface between them was also observed. Samples that contain the *m*-$BiVO_4$ and *t*-$BiVO_4$ phases exhibited better photocatalytic performance for MB degradation under visible irradiation than that of the isolated phases. The *m*-$BiVO_4$/*t*-$BiVO_4$ heterostructure showed no significant deactivation even after four successive re-uses for MB photodegradation. Oxidation mechanism of the MB dye was elucidated by mass spectroscopy. The photoactivity enhancement in the *m*-$BiVO_4$/*t*-$BiVO_4$ sample was due to the formation of a suitable heterojunction between the $BiVO_4$ phases, promoting the effective separation of photogenerated charges. The experiments using active scavenger species and the VB top analysis based on XPS indicated the formation of a type-II heterostructure where the increase in the charge carrier lifetime enabled the formation of active species. In addition, holes ($h^+$), superoxide anion radicals ($O_2^{-\bullet}$) and hydroxyl radicals ($^\bullet$OH) were the primary active species responsible for MB photodegradation.

## Acknowledgements

The authors are grateful to the FAPESP (Under grants no. 13/13888-0 and 14/09014-7), CNPq (Under grants no. 300247/2013-3), CAPES and FINEP for financial support. We are grateful to Msc. Pablo S. Lemos (LIEC/UFSCar Brazil), B.Chem. Fellipe M. Cadan and Prof. Dr. Eduardo B. Azevedo (IQSC/USP) for help with the DRS UV–vis and TOC analyzer facilities, respectively. We are also grateful to the Laboratory for Research in Energy and Materials—Brazilian Nanotechnology National Laboratory (LNNano) for technical support with the X-ray photoelectron spectroscopy work (Under grants n° XPS-18304), and to the Structural Characterization Laboratory (LCE, DEMa) for technical support with the HRTEM work.

## Appendix A. Supplementary data

Supplementary data associated with this article can be found, in the online version, at http://dx.doi.org/10.1016/j.apcatb.2016.01.065.

## References

[1] Y. Park, K.J. McDonald, K.-S. Choi, Chem. Soc. Rev. 42 (2013) 2321–2337.
[2] S.J.A. Moniz, S.A. Shevlin, D.J. Martin, Z.-X. Guo, J. Tang, Energy Environ. Sci. 8 (2015) 731–759.
[3] Q. Li, B. Guo, J. Yu, J. Ran, B. Zhang, H. Yan, J.R. Gong, J. Am. Chem. Soc. 133 (2011) 10878–10884.
[4] K. Sridharan, E. Jang, T.J. Park, Appl. Catal. B: Environ. 142–143 (2013) 718–728.
[5] G. Wu, S.S. Thind, J. Wen, K. Yan, A. Chen, Appl. Catal. B: Environ. 142–143 (2013) 590–597.
[6] K. Sayama, K. Mukasa, R. Abe, Y. Abe, H. Arakawa, J. Photochem. Photobiol. A: Chem. 148 (2002) 71–77.
[7] Z. Zou, J. Ye, K. Sayama, H. Arakawa, Nature 414 (2001) 625–627.
[8] W. Hou, W.H. Hung, P. Pavaskar, A. Goeppert, M. Aykol, S.B. Cronin, ACS Catal. 1 (2011) 929–936.
[9] S. Obregón, A. Caballero, G. Colón, Appl. Catal. B: Environ. 117–118 (2012) 59–66.
[10] S. Obregón, G. Colón, J. Mol. Catal. A: Chem. 376 (2013) 40–47.
[11] W. Wang, X. Huang, S. Wu, Y. Zhou, L. Wang, H. Shi, Y. Liang, B. Zou, Appl. Catal. B: Environ. 134–135 (2013) 293–301.
[12] S. Sun, W. Wang, D. Li, L. Zhang, D. Jiang, ACS Catal. 4 (2014) 3498–3503.
[13] G. Li, Y. Bai, W.F. Zhang, Mater. Chem. Phys. 136 (2012) 930–934.
[14] Y. Guo, X. Yang, F. Ma, K. Li, L. Xu, X. Yuan, Y. Guo, Appl. Surf. Sci. 256 (2010) 2215–2222.
[15] A. Kudo, K. Omori, H. Kato, J. Am. Chem. Soc. 121 (1999) 11459–11467.
[16] S. Tokunaga, H. Kato, A. Kudo, Chem. Mater. 13 (2001) 4624–4628.
[17] O.F. Lopes, K.T.G. Carvalho, G.K. Macedo, V.R. de Mendonça, W. Avansi, C. Ribeiro, New J. Chem. 39 (2015) 6231–6237.
[18] X. Chen, S. Shen, L. Guo, S.S. Mao, Chem. Rev. 110 (2010) 6503–6570.
[19] L. Ye, J. Liu, C. Gong, L. Tian, T. Peng, L. Zan, ACS Catal. 2 (2012) 1677–1683.
[20] X. Yang, H. Cui, Y. Li, J. Qin, R. Zhang, H. Tang, ACS Catal. 3 (2013) 363–369.
[21] S.K. Pilli, T.E. Furtak, L.D. Brown, T.G. Deutsch, J.A. Turner, A.M. Herring, Energy Environ. Sci. 4 (2011) 5028.
[22] A. Zhang, J. Zhang, J. Hazard. Mater. 173 (2010) 265–272.
[23] F. Zhou, Y. Min, J. Fan, Q. Xu, Chem. Eng. J. 266 (2015) 48–55.
[24] A. Zhang, J. Zhang, Appl. Surf. Sci. 256 (2010) 3224–3227.
[25] F. Lin, D. Wang, Z. Jiang, Y. Ma, J. Li, R. Li, C. Li, Energy Environ. Sci. 5 (2012) 6400–6406.
[26] J. Yang, D. Wang, H. Han, C. Li, Acc. Chem. Res. 46 (2013) 1900–1909.
[27] Y. Hu, D. Li, Y. Zheng, W. Chen, Y. He, Y. Shao, X. Fu, G. Xiao, Appl. Catal. B: Environ. 104 (2011) 30–36.
[28] P. Chatchai, Y. Murakami, S. Kishioka, A.Y. Nosaka, Y. Nosaka, Electrochim. Acta 54 (2009) 1147–1152.
[29] P. Madhusudan, J. Ran, J. Zhang, J. Yu, G. Liu, Appl. Catal. B: Environ. 110 (2011) 286–295.
[30] H. Fan, T. Jiang, H. Li, D. Wang, L. Wang, J. Zhai, D. He, P. Wang, T. Xie, J. Phys. Chem. C 116 (2012) 2425–2430.
[31] G. Tan, L. Zhang, H. Ren, S. Wei, J. Huang, A. Xia, ACS Appl. Mater. Interfaces 5 (2013) 5186–5193.
[32] S. Usai, S. Obregon, A.I. Becerro, G. Colon, J. Phys. Chem. C 117 (2013) 24479–24484.
[33] S. Obregon, S.W. Lee, G. Colon, Dalton Trans. 43 (2014) 311–316.
[34] Y. Xue, X. Wang, Int. J. Hydrogen Energy 40 (2015) 5878–5888.
[35] W. Avansi, V.R. de Mendonça, O.F. Lopes, C. Ribeiro, RSC Adv. 5 (2015) 12000–12006.
[36] O.F. Lopes, E.C. Paris, C. Ribeiro, Appl. Catal. B: Environ. 144 (2014) 800–808.

[37] O.F. Lopes, V.R. de Mendonça, F.B.F. Silva, E. Paris, C. Ribeiro, Quim. Nova 38 (2015) 106–117.
[38] E.R. Camargo, M.G. Dancini, M. Kakihana, J. Mater. Res. 29 (2014) 131–138.
[39] H.A.J.L. Mourão, O.F. Lopes, A.R. Malagutti, E.C. Paris, C. Ribeiro, Mater. Sci. Semicond. Process. 25 (2014) 320–329.
[40] J.-Y. Piquemal, E. Briot, J.-M. Brégeault, Dalton Trans. 42 (2013) 29–45.
[41] I.A. de Castro, W. Avansi, C. Ribeiro, CrystEngComm 16 (2014) 1514–1524.
[42] W. Avansi, R. Arenal, V.R. de Mendonça, C. Ribeiro, E. Longo, CrystEngComm 16 (2014) 5021–5027.
[43] W. Avansi, C. Ribeiro, E.R. Leite, V.R. Mastelaro, Mater. Chem. Phys. 127 (2011) 56–61.
[44] W. Avansi, C. Ribeiro, E.R. Leite, V.R. Mastelaro, Cryst. Growth Des. 9 (2009) 3626–3631.
[45] Y. Li, J. Wang, H. Yao, L. Dang, Z. Li, J. Mol. Catal. A: Chem. 334 (2011) 116–122.
[46] K. Ishibashi, A. Fujishima, J. Photochem. Photobiol. A: Chem. 134 (2000) 139–142.
[47] K. Ishibashi, A. Fujishima, Electrochem. Commun. 2 (2000) 207–210.
[48] M. Nag, S. Ghosh, R.K. Rana, S.V. Manorama, J. Phys. Chem. Lett. 1 (2010) 2881–2885.
[49] A.B. Murphy, Sol. Energy Mater. Sol. Cells 91 (2007) 1326–1337.
[50] J. Yu, A. Kudo, Adv. Funct. Mater. 16 (2006) 2163–2169.
[51] V.R. de Mendonça, H.A.J.L. Mourão, A.R. Malagutti, C. Ribeiro, Photochem. Photobiol. 90 (2014) 66–72.
[52] Y. Cao, T. He, Y. Chen, Y. Cao, J. Phys. Chem. C 114 (2010) 3627–3633.
[53] T. Guohui, F. Honggang, J. Liqiang, X. Baifu, P. Kai, J. Phys. Chem. C 112 (2008) 3083–3089.
[54] Z. Ding, G.Q. Lu, P.F. Greenfield, J. Phys. Chem. B 104 (2000) 4815–4820.
[55] D.C. Hurum, A.G. Agrios, K.A. Gray, T. Rajh, M.C. Thurnauer, J. Phys. Chem. B 107 (2003) 4545–4549.
[56] K. Ding, B. Chen, Z. Fang, Y. Zhang, Theor. Chem. Acc. 132 (2013) 1–7.
[57] V.R. de Mendonça, O.F. Lopes, R.P. Fregonesi, T.R. Giraldi, C. Ribeiro, Appl. Surf. Sci. 298 (2014) 182–191.
[58] H.A.J.L. Mourão, W. Avansi Jr., C. Ribeiro, Mater. Chem. Phys. 135 (2012) 524–532.
[59] J. Cai, Y. Zhu, D. Liu, M. Meng, Z. Hu, Z. Jiang, ACS Catal. 5 (2015) 1708–1716.
[60] V.-I. Merupo, S. Velumani, K. Ordon, N. Errien, J. Szade, A.-H. Kassiba, CrystEngComm 17 (2015) 3366–3375.
[61] M. Wang, H. Zheng, J. Liu, D. Dong, Y. Che, C. Yang, Mater. Sci. Semicond. Process. 30 (2015) 307–313.
[62] B. Ohtani, O.O. Prieto-Mahaney, D. Li, R. Abe, J. Photochem. Photobiol. A: Chem. 216 (2010) 179–182.
[63] V. Subramanian, E. Wolf, P. Kamat, J. Phys. Chem. B 107 (2003) 7479–7485.
[64] L. Zhang, J. Long, W. Pan, S. Zhou, J. Zhu, Y. Zhao, X. Wang, G. Cao, Mater. Chem. Phys. 136 (2012) 897–902.
[65] H. Tong, S. Ouyang, Y. Bi, N. Umezawa, M. Oshikiri, J. Ye, Adv. Mater. 24 (2012) 229–251.
[66] A. Kudo, Y. Miseki, Chem. Soc. Rev. 38 (2009) 253–278.
[67] D. Ke, T. Peng, L. Ma, P. Cai, P. Jiang, Appl. Catal. A: Gen. 350 (2008) 111–117.
[68] K.M.M. Abou El-Nour, A. Eftaiha, A. Al-Warthan, R.A.A. Ammar, Arab. J. Chem. 3 (2010) 135–140.
[69] Y. Liu, B. Huang, Y. Dai, X. Zhang, X. Qin, M. Jiang, M.H. Whangbo, Catal. Commun. 11 (2009) 210–213.
[70] T.C. Ramalho, L.C.A. Oliveira, K.T.G. Carvalho, E.F. Souza, E.F.F. Cunha, M. Nazzaro, J. Mater. Sci. 43 (2008) 5982–5988.
[71] T.C. Ramalho, L.C.A. Oliveira, K.T.G. Carvalho, E.F. Souza, E.F.F. da Cunha, M. Nazzaro, Mol. Phys. 107 (2009) 171–179.
[72] K.T.G. Carvalho, A.C. Silva, L.C.A. Oliveira, M. Goncalves, Z.M. Magriotis, Quim. Nova 32 (2009) 1373–1377.
[73] A.A. Tireli, I.D.R. Guimarães, J.C.D.S. Terra, R.R. da Silva, M.C. Guerreiro, Environ. Sci. Pollut. Res. Int. 22 (2014) 870.
[74] T. Zhang, T. Oyama, A. Aoshima, H. Hidaka, J. Zhao, N. Serpone, J. Photochem. Photobiol. A: Chem. 140 (2001) 163–172.
[75] J. Cao, B. Xu, B. Luo, H. Lin, S. Chen, Catal. Commun. 13 (2011) 63–68.
[76] M. Yin, Z. Li, J. Kou, Z. Zou, Environ. Sci. Technol. 43 (2009) 8361–8366.
[77] Y. Zhao, C. Eley, J. Hu, J.S. Foord, L. Ye, H. He, S.C.E. Tsang, Angew. Chemie Int. Ed. 51 (2012) 3846–3849.
[78] W.Y. Teoh, J.A. Scott, R. Amal, J. Phys. Chem. Lett. 3 (2012) 629–639.